DOI: 10.13009/EUCASS2022-4397
9TH EUROPEAN CONFERENCE FOR AERONAUTICS AND SPACE SCIENCES (EUCASS)

Preliminary CFD analysis of an innovative hybrid HAPS configuration

Vincenzo Rosario Baraniello and Giuseppe Persechino***
**CIRA – Italian Aerospace Research Centre*
Via Maiorise, Capua (CE) Italy
***CIRA – Italian Aerospace Research Centre*
Via Maiorise, Capua (CE) Italy

Abstract
CIRA is designing an innovative HAPS. The selected configuration can generate both aerodynamic and aerostatic forces. A hybrid HAPS represents itself a novelty while some hybrid aerostats have been proposed for tropospheric applications. In this paper, the authors will present the results of a preliminary CFD analysis performed on the designed configuration using the open source solver OpenFoam. Several simulations at different angles of attack and sideslip have been carried out in order to investigate the steady-state air motion around the HAPS at the nominal mission altitude. Finally, typical aerodynamic force and moment coefficients have been computed.

1. Introduction

CIRA is currently designing an innovative HAPS configuration for Earth Observation and telecommunications named High Altitude Hybrid Airship. The designed configuration can generate both aerodynamic and aerostatic forces to balance the weight during the different phases of a mission. The design of a hybrid configuration for stratospheric platforms represents itself a novelty in the aerospace sector while some hybrid platforms have been already proposed only for tropospheric applications.
The interest in long endurance unmanned stratospheric platforms (also known as HAPS: high altitude pseudo satellites) has increased in the last years. Some applications are proposed in [1], [2], [3], [4].
These applications concern essentially Earth Observation and telecommunications. From an altitude of 20 km, HAPS will be able to view an area on ground having a diameter of about 70 km with optical sensors and 140 km with radar. This flight altitude offers greater proximity to the Earth surface providing imagery at greater spatial resolution than satellite imagery.
HAPS represent thus a complementary solution to satellites but also to RPAS. In comparison to satellites, as explained, they allow observation of a less extended area (local scale) but with greater resolution and lower revisit time than satellites. Moreover, they are able to maintain station (station-keeping) on a predefined area (at a significantly lower altitude than geostationary satellites). Maintenance and updating of their equipment and payload are also possible because platforms can land and take-off again.
A fleet of RPAS could also guarantee local scale coverage, but in this case, the complexity of the system, in terms of management and maintenance, is greater in comparison to single HAPS.
Current HAPS proposals can be generally classified in LTA platforms or HTA fixed wing platforms. As explained in [5], both these solutions cannot optimally cover the payload range from 25 up to 100 kg, but this payload range is very interesting for several applications.
A hybrid HAPS will enable the possibility to have a payload capability from 25 up to 100 kg, while limiting the size and the overall weight of the platform. The reduction of the weight is a consequence of the possibility to remove or strongly reduce the volume of the ballonets, realizing, however, a HAPS, which can be recoverable and reusable thanks to aerodynamic lift.
Thanks to an optimal conceptual design process, we have achieved a configuration of our hybrid HAPS based on a lenticular shape with an overall weight of about 180kg and a volume equal to 1220 m3, which can embark a payload having a weight of 25 kg [6].
This conceptual design process is based on the use of semi-empirical formula to compute aerodynamic parameters.
Thus, in order to validate the results of the conceptual design phase, a preliminary, but complete, CFD analysis has been performed on the lenticular configuration.

DOI: 10.13009/EUCASS2022-4397

In fact, the CFD analyses allowed to improve the conceptual design, obtaining a final configuration able to carry on the same initial desired payload (in terms of weight) but having reduced overall weight and dimensions.
The paper will be organized in two main parts. In the first part we will briefly present the structure and the results of the conceptual design process we have implemented to obtain several candidate configurations, from whom we have selected the final one which is the object of the analysis of this paper; while, in the second part, we will show and discuss the results of the aerodynamic analyses.
In the conclusion of the paper we will also provide to the readers a first overview of the next steps in our design process.

2. Summary of the conceptual design process

In order to generate the layout of the HAPS concept, the authors have implemented a conceptual design tool based on two steps [6]. This tool allows to design with great precision the layout and, at the same time, it provides an assessment of the mass breakdown.
The first step provides, as result, a preliminary geometry definition and overall mass estimation, while the second one provides the final layout and a more accurate mass breakdown assessment.
The authors have implemented the first step in Matlab® while the second step in the SW Rhinoceros®, which is an environment for tri-dimensional modelling of surfaces and it has several plugins to perform other operations on the designed geometry.
The authors have used the plugin Grasshopper to compute the masses of the sub-systems and aerodynamic parameters using semi-empirical expressions or CFD results.
In this plugin, the authors have also implemented calculations to verify that generated buoyancy and aerodynamic lift, at the nominal flight conditions, can balance the weight.
A schematic representation of this conceptual design loop is reported in Figure 1.
This tool has been used to generate a HAPS layout, starting from the mission requirements reported in **Table 1**.

Table 1: Mission Requirements

Payload	25 Kg (at least 12% of the MTOW)
Mission Altitude	18000-20000 m
Mission Duration	4 months
Mission Speed	16 m/sec
Mission Theatre	Mediterrean Sea
HAPS Mass Category	<300 Kg
Night Duration	15 hours (January)
Energy Source	Photovoltaic associated with batteries

The tool provides, as best result, the lenticular shape reported in Figure 2, whose dimensions are reported in **Table 2**.

Table 2: HAPS dimensions, lenticular layout

w [m]	**l [m]**	**h [m]**	**Volume [m^3]**	**S [m^2]**
14	29	5.75	1210	304

This configuration has a final weight of about 183 kg and a buoyancy ratio of 0.81 which means that the 81% of the lift is due to aerostatic forces.

DOI: 10.13009/EUCASS2022-4397

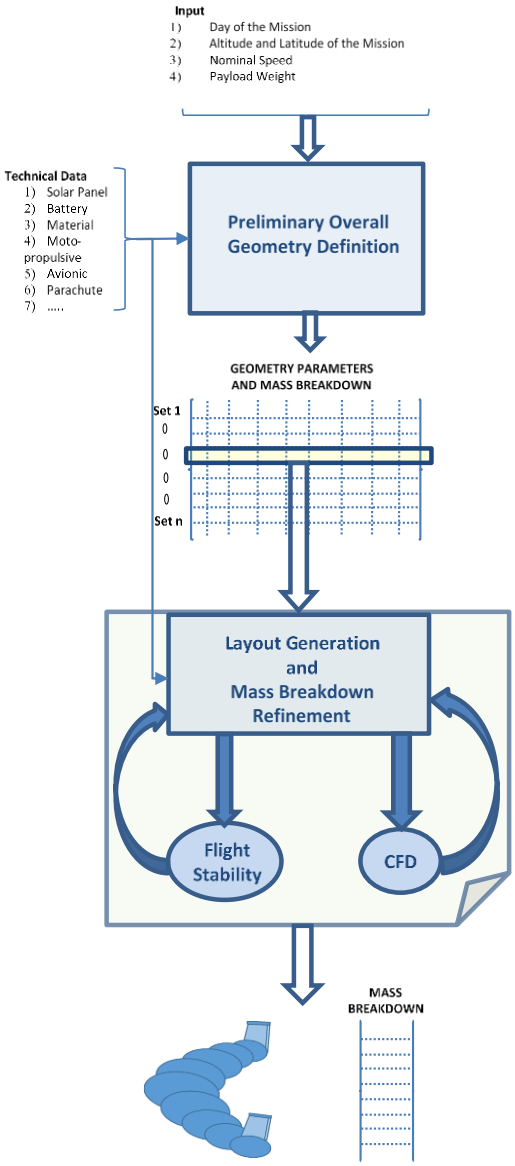

Figure 1: Schematic representation of the conceptual design process

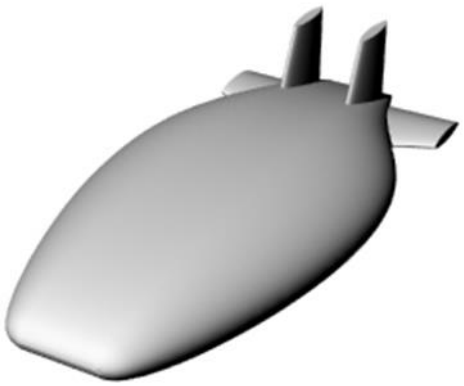

Figure 2: HAPS lenticular layout

DOI: 10.13009/EUCASS2022-4397

3. Aerodynamic analysis

3.1 Introduction

In this section we will describe the results of a preliminary CFD analysis required to assess the features of the flow field around the platform and to achieve a first estimation of the aerodynamic coefficients, which can be used to improve the results of the design process and/or to build an aerodynamic database which will be used in the flight dynamic model of the platform. For the sake of simplicity, neither nacelles nor propeller or payload bays have been considered in this analysis.
The aerodynamic coefficients allow also an assessment of the static stability of the platform.
The CFD analyses have been carried out on the open source tool OpenFOAM® using its the steady-state solver SimpleFOAM based on Semi-Implicit Method for Pressure Linked Equations [7].
Solution control is addressed by implicit under-relaxation factors. Default settings are considered for them in the flow field simulations.
The authors have built the aerodynamic mesh starting from the CAD geometry generated by the conceptual design tool which is also based on the use of Rhino® and Grasshopper, using the mesh generation utilities blockmesh and snappyHexMesh. The snappyHexMesh utility generates 3-dimensional meshes containing hexahedra (hex) and split-hexahedra (split-hex) automatically from triangulated surface geometries, or tri-surfaces, in Stereolithography (STL) or Wavefront Object (OBJ) format [8].
Flow field conditions at an altitude equal to 18000 m have been generated, simulating an airspeed equal to 16 m s^{-1}.
These conditions represent the nominal altitude and airspeed, the platform has been designed for.
Air has been modelled as a perfect gas with a dynamic viscosity equal to 1.18x10-4 m^2 s^{-1}.
RANS modelling is based on Shear Stress Transport (SST) k-ω model.
The analyses have been performed at several angles of attack [0°÷17°] and sideslip [0°, -10°, -20°, -30°].
Reynolds number, refereed to the length of the hull, is about 4,000,000.
The hull of the platform has been realized using symmetric 6-digit NACA airfoils.

3.2 Analysis of the flow field around the platform

In this paragraph, the authors present some considerations about the flow field around the lenticular HAPS platform at several angles attack and sideslip as well as airspeed distribution along with selected spanwise locations are evaluated and compared.
Flow field computations have been carried out on a hybrid grid generated by the openfoam function blockmesh (structured grid) and refined around the plane with the snappyhexmesh function (unstructured grid). This grid is essential based on the use of hexaedra, polyhedra and prisms.
The authors have reported a detail of the mesh close to the aircraft in Figure 3.

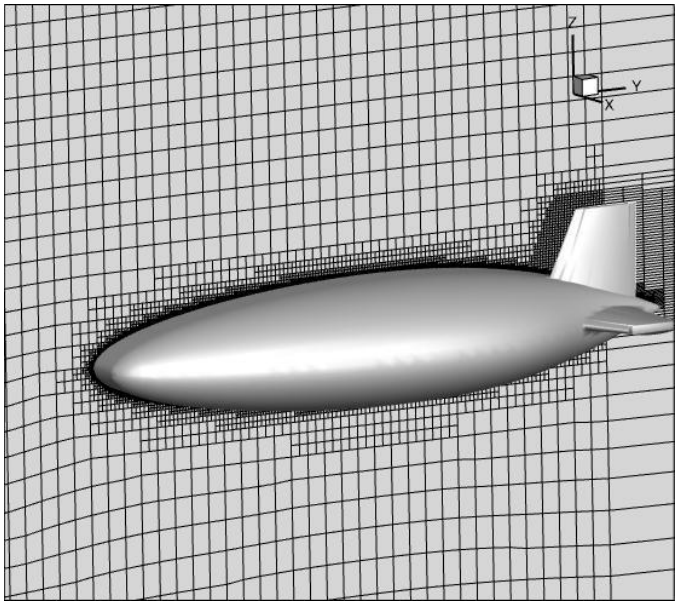

Figure 3: Details of the mesh close to the aircraft

DOI: 10.13009/EUCASS2022-4397

In this section, the reference axes are parallel to the wind tunnel axis, where “Z” axis is vertical, “Y” and “X” lie in the horizontal plane: “Y” in the direction of the flow while “X” is perpendicular to both “Y” and “Z”.
In the next figures the authors will report the 2-D flow field in some planes of great importance.
In Figure 4 the graphic representation of the positions of these cutting planes are reported. The exact location of each plane is indicated in Table 3.

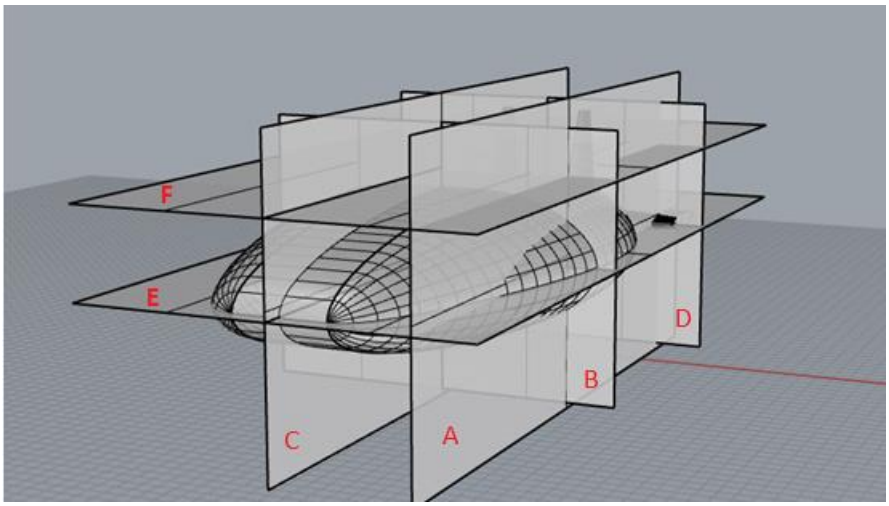

Figure 4: Cutting Planes

Table 3: Position of the cutting planes

Plane ID	Description
A	Parallel to YZ symmetry plane, located at 5.5 m far from it.
B	XZ plane, located at 14.5 m far from the nose of the platform
C	YZ symmetry plane
D	Parallel to XZ plane, located at 26 m far from the nose of the platform
E	XY Plane
F	Parallel to XY Plane, located at 4 m toward the top of the platform

Figure 5 and Figure 6 represent the 2-D flow field, in sections “C” and “A”, at zero angle of attack and zero angle of sideslip. In Figure 5, which represents the section in the plane of symmetry YZ, you can see the stagnation point located at the nose of the platform, the symmetry of flow field along the upper and lower parts of the airfoil, with an exception in the rear part, where the presence of the tail induces an acceleration to the air in upper part of the platform.
Figure 6 represents the flow field in a section located at 5.5 meters from the symmetry plane. It is interesting to note that the flow has not a stagnation point in the area of the leading edge. This is due to the lenticular shape which has a behavior similar to a sweptback wing, inducing a lateral component of the airspeed even if the sideslip angle is equal to zero.
The horizontal stabilizer is partially in the wake of the hull. A stagnation point is here available in the area of the leading edge.
Figure 7 and Figure 8 represent the 2-D flow field respectively in the “E” plane and in the “C” plane, with an angle of attack equal to 8°. The stagnation point is present only for the airfoils in the central zone of the hull which is perpendicular to the airstream, for the lateral sections, as explained, the airstream follows the lenticular shape. In the ZY plane, the lenticular shape represents itself an airfoil. In fact, considering the absence of the sideslip angle, the flow field is symmetric. After the zone of the hull maximum width, the lenticular shape leads the airstream in a direction which is quite perpendicular to the leading edge of the stabilizer.
The low speed zone between the horizontal stabilizer and hull maximum width seems to be caused by both the wake of the hull and the presence of the stabilizer itself (subsonic flow).
Figure 8 represents the flow field in the YZ symmetry plane. Due to the positive angle of attack, the stagnation point moves to the lower part of the airfoil. In the upper part of the airfoil the expansion is greater than in the lower part.

DOI: 10.13009/EUCASS2022-4397

Figure 9 and Figure 10 report the flow field in the area between the two vertical components of the tail (cutting planes "D" and "F"). As explained before, the vertical surfaces of the tail induce an acceleration to the airstream.
In Figure 11 and Figure 12 an example of flow field with a sideslip angle is reported. The magnitude of the sideslip angle is 20° degrees and the airflow comes from the left (negative X direction).
In both the figures, it is possible to note the asymmetry of the flow field in right and left part of the platform, with a low airspeed area in the right part starting from maximum width of section. This is representative of a wake due to the sideslip. As stated before, the in-plane section of the hull is itself an airfoil. When the airspeed has a lateral component, on the upper part an expansion of the air is present with a separation in the rear part due to the high value of the sideslip angle.
In the Figure 13, Figure 14 and Figure 15 the authors have reported the streamlines around the plane at an agle of attack equal to 8° without sideslip. It is possible to note the effect of the lenticular shape of the platform inducing a lateral curvature on the streamlines.

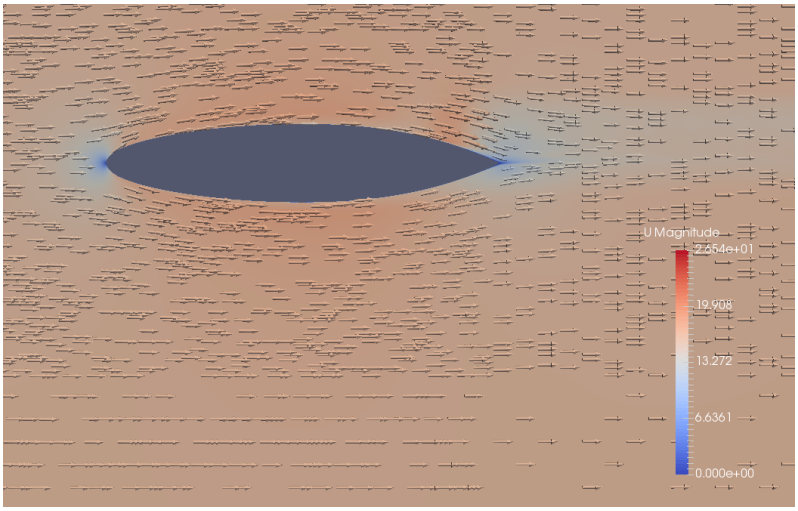

Figure 5: Flow field in the "C" cutting plane at α=0°, β=0°

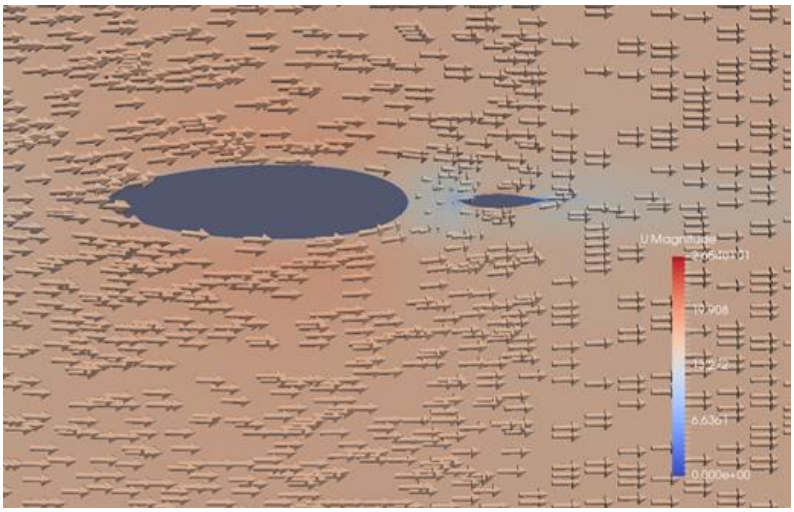

Figure 6: Flow field in the "A" cutting plane at α=0°, β=0°

DOI: 10.13009/EUCASS2022-4397

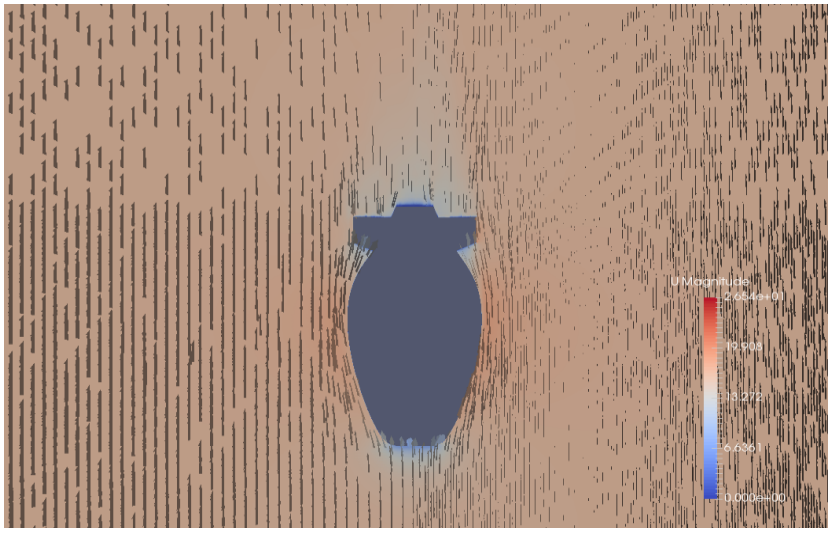

Figure 7: Flow field in the “E” cutting plane at α=8°, β=0°

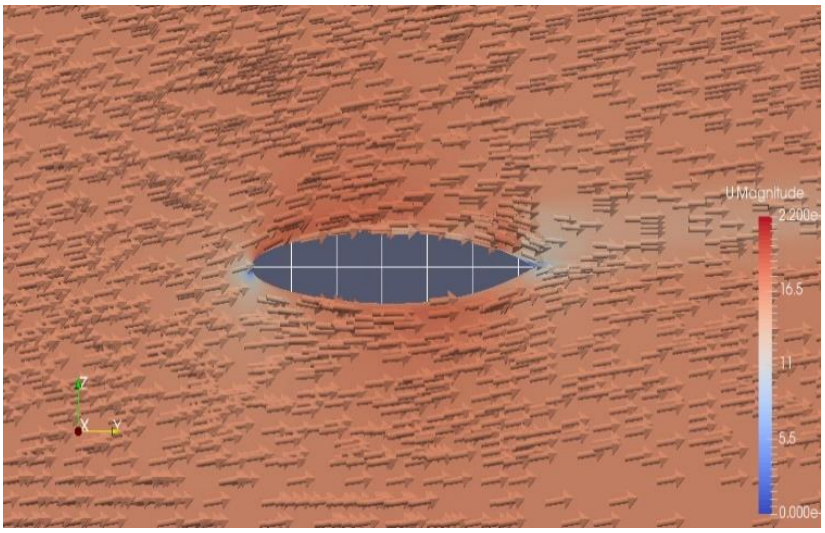

Figure 8: Flow field in the “C” cutting plane at α=8°, β=0°

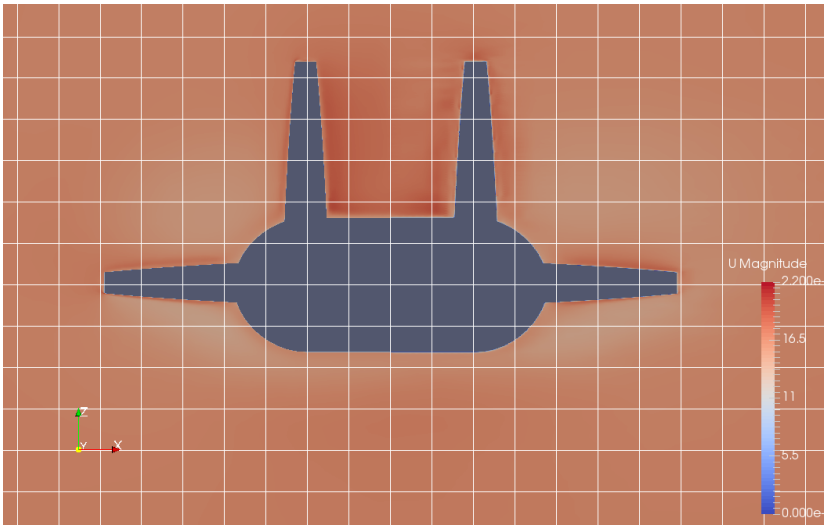

Figure 9: Flow field in the “D” cutting plane at α=8°, β=0°

DOI: 10.13009/EUCASS2022-4397

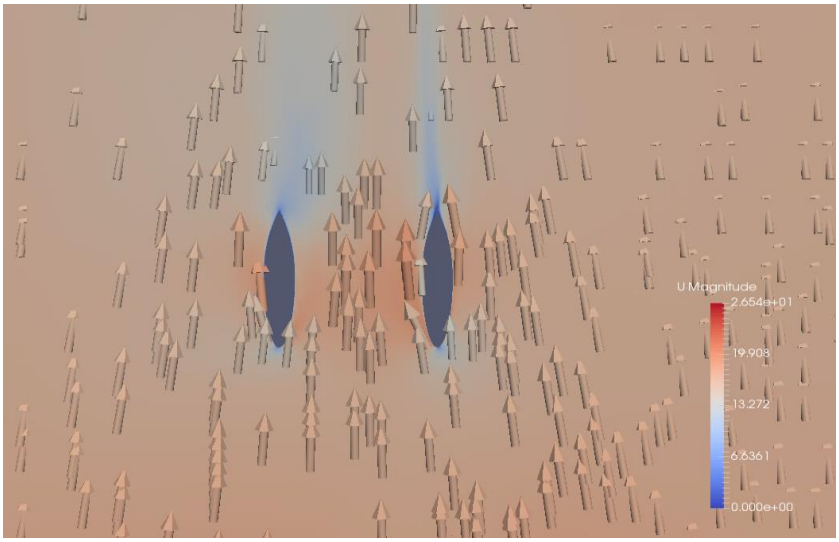

Figure 10: Flow field in the “F” cutting plane at α=8°, β=0°

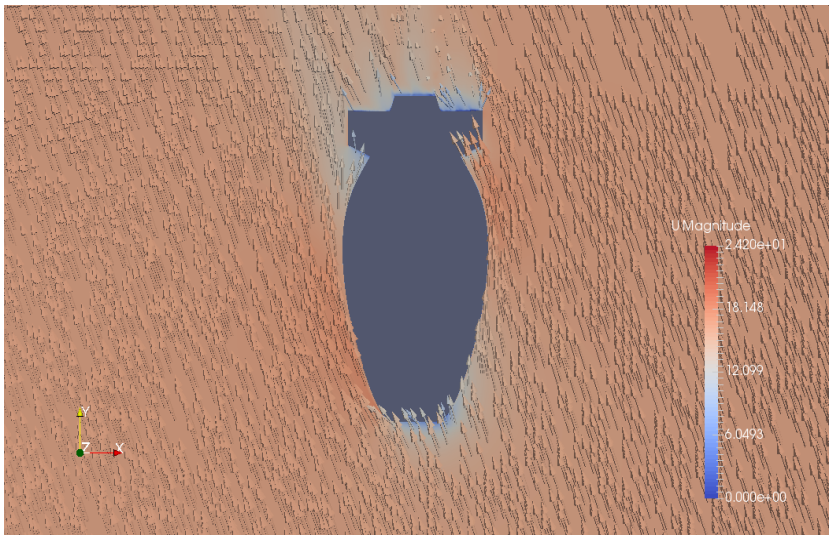

Figure 11: Flow field in the “E” cutting plane at α=8°, β=-20°

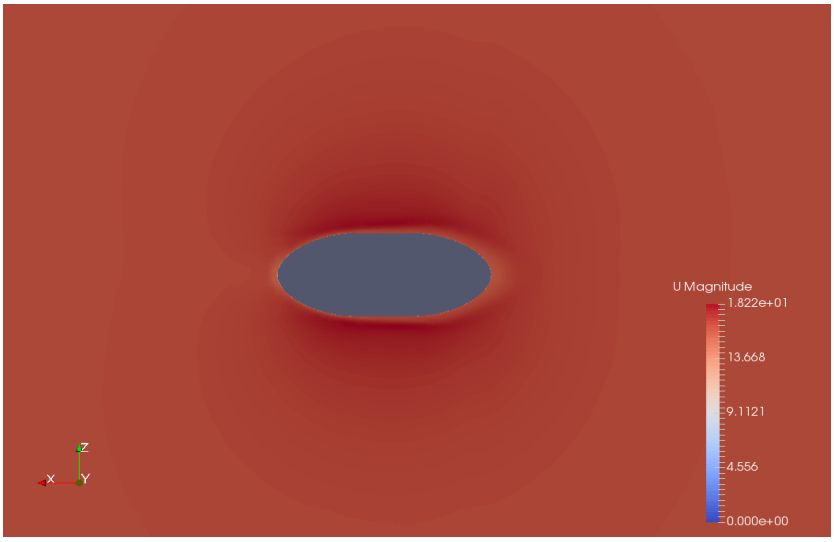

Figure 12: Flow field in the “B” cutting plane at α=8°, β=-20°

DOI: 10.13009/EUCASS2022-4397

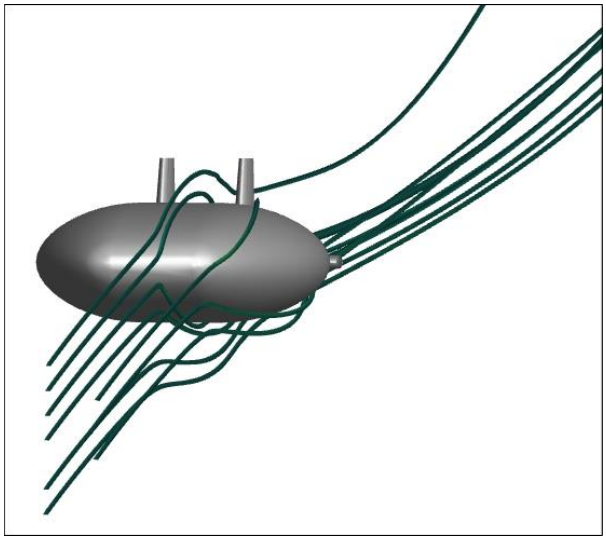

Figure 13: Streamlines α=8°, β=0°

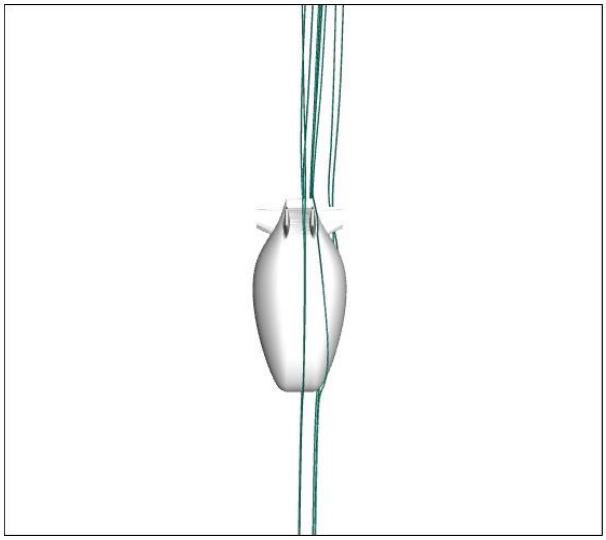

Figure 14: Streamlines α=8°, β=0°

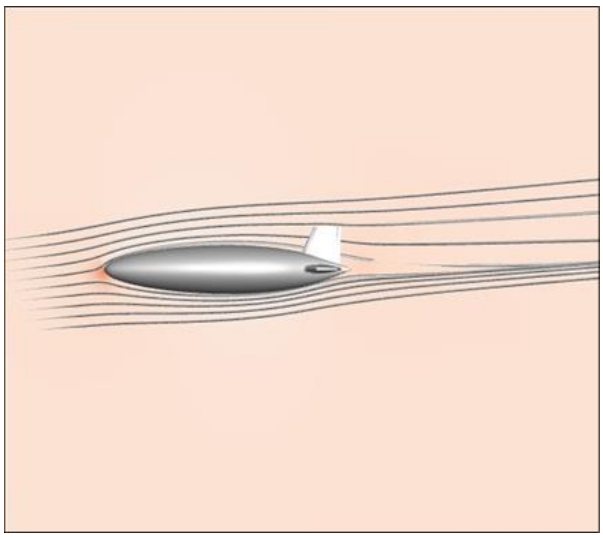

Figure 15: Streamlines α=8°, β=0°

DOI: 10.13009/EUCASS2022-4397

3.3 Aerodynamic coefficients

In this paragraph the authors will summarize the main aerodynamic coefficients respect to wind axes, computed from the simulation at different angles of attack and sideslip. Four different values of the sideslip angle are considered: [-30°, - 20°, -10°, 0°].
The computed coefficients are referred to the in-plane area of the platform reported in Table 2.
In Figure 16 the lift coefficient versus the angle-of-attack is reported. The zero-lift coefficient is practically zero and this due to the symmetric shape of the hull and the wing. Increasing the sideslip angle, there is a very slight variation in the slope of this coefficient.
The stall behavior has not been investigated.
The lift coefficient can be approximated by a linear expression (1) whose slope depends on the sideslip angle (2).

$$C_L(\alpha,\beta) = C_{L_\alpha}(\beta) \times \alpha \quad \textbf{(1)}$$

$$C_{L_\alpha}(\beta) = -0.0001 \times \beta + 0.013 \quad \textbf{(2)}$$

The value of the lift coefficient slope C_{L_α}at zero sideslip is coherent also with semi-empirical Jones formula (3) described in [9] which is quite accurate when AR <1. The AR for the hybrid platform can be computed as width-to-surface ratio and is equal to 0.52.

$$C_{L_\alpha}(\beta = 0°) = \frac{\pi \times AR}{2} \times \frac{\pi}{180} = 0.014\ [1/°] \quad \textbf{(3)}$$

In Figure 17 the drag polar is reported in terms of drag and lift coefficients. The effect of the sideslip can be seen by the variation in both: the zero-lift drag and the curvature of the polar at higher angles of sideslip.
At higher values of the sideslip angles, the influence of the wake drag becomes predominant and greater than the contribution of the lift dependent drag.
In the equations (4), (5), (6) and (7) the authors have reported the expressions of the drag coefficients at different sideslip angles.

$$C_D(\beta = 0°) = 0.023 + 0.8 \times (C_L)^2 \quad \textbf{(4)}$$

$$C_D\ (|\beta| = 10°) = 0.028 + 0.8 \times (C_L)^2 \quad \textbf{(5)}$$

$$C_D(|\beta| = 20°) = 0.041 + 0.7 \times (C_L)^2 \quad \textbf{(6)}$$

$$C_D(|\beta| = 30°) = 0.068 + 0.53 \times (C_L)^2 \quad \textbf{(7)}$$

An approximate expression for the zero-lift drag coefficient C_{D_0}versus the sideslip angle is reported in (8).

$$C_{D_0} = 0.023 + 0.00005 \times |\beta| \quad \textbf{(8)}$$

In Figure 18 the side force coefficient versus the angle of attack at several sideslip angles is reported.
In Figure 19 the rolling moment coefficient versus the angle of attack at several sideslip angles is reported.
In Figure 20 the pitching moment coefficient versus the angle of attack at several sideslip angles is reported.
In Figure 21 the yaw moment coefficient versus the angle of attack at several sideslip angles is reported.

DOI: 10.13009/EUCASS2022-4397

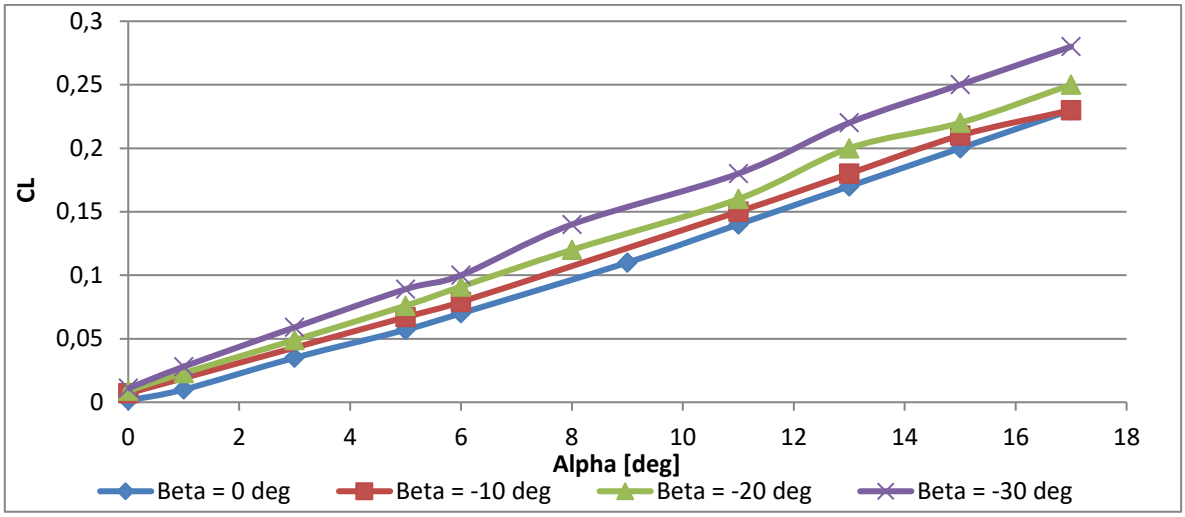

Figure 16: Lift coefficient versus angle-of-attack at several angles of sideslip

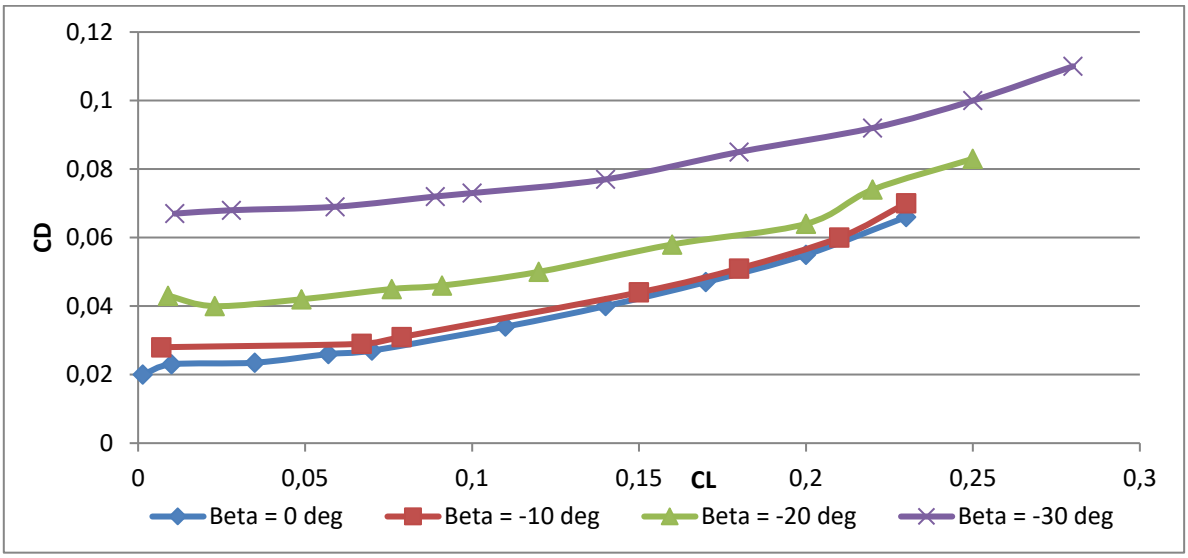

Figure 17: Drag coefficient versus Lift coefficient at several angles of sideslip

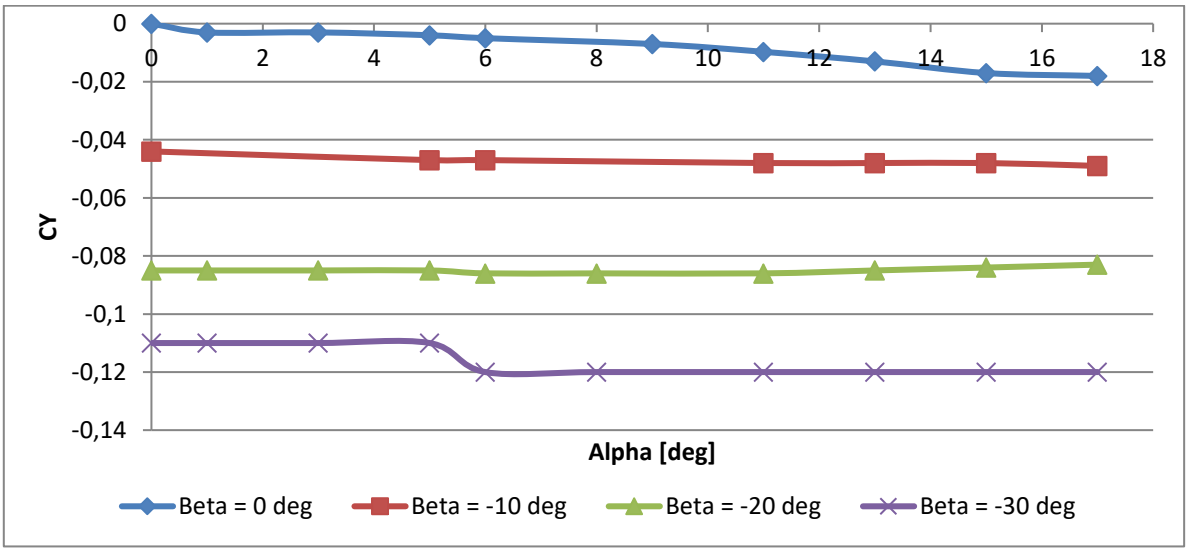

Figure 18: Side Force coefficient versus angle-of-attack at several angles of sideslip

DOI: 10.13009/EUCASS2022-4397

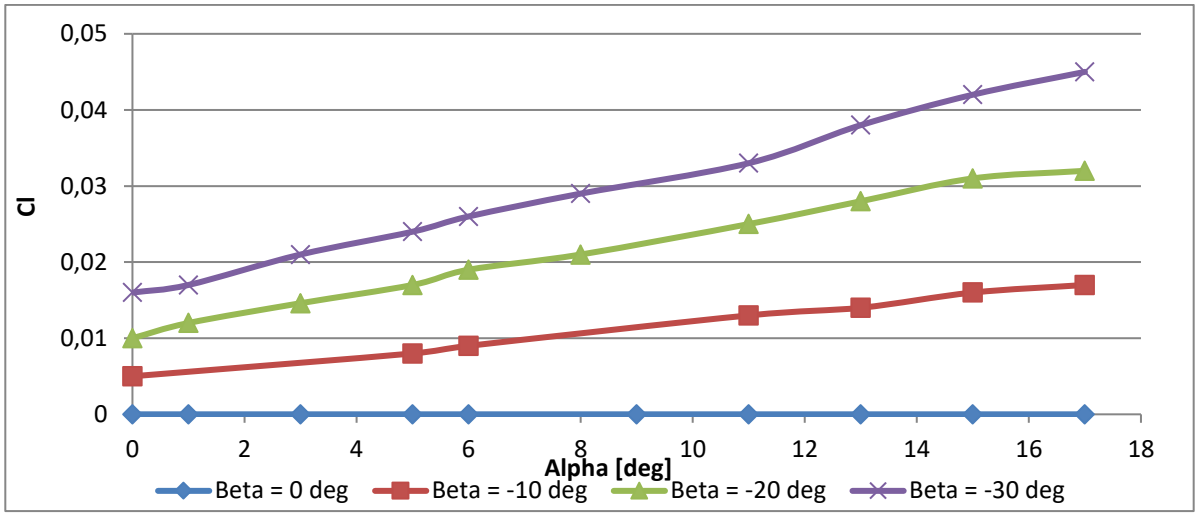

Figure 19: Rolling moment coefficient versus angle-of-attack at several angles of sideslip

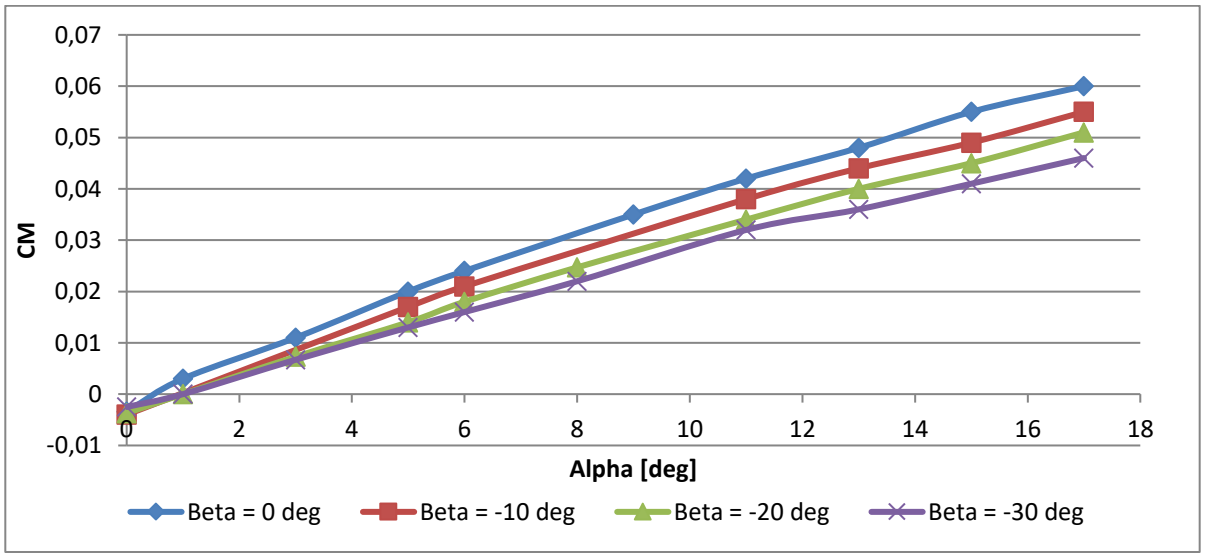

Figure 20: Pitching moment coefficient versus angle-of-attack at several angles of sideslip

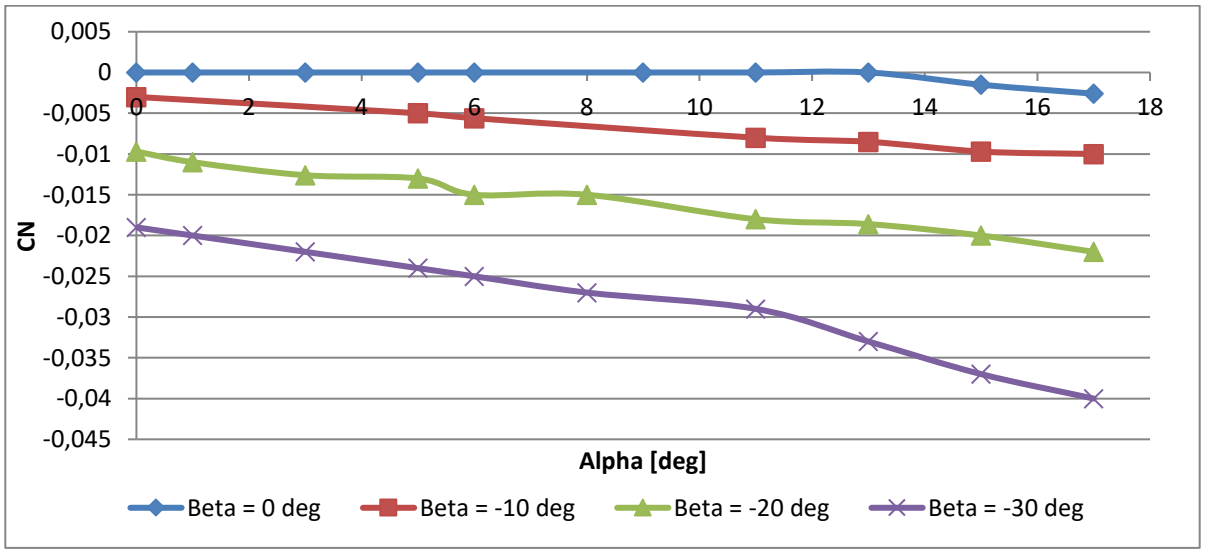

Figure 21: Yaw moment coefficient versus angle-of-attack at several angles of sideslip

DOI: 10.13009/EUCASS2022-4397

4. Conclusion

In this paper the authors have presented the results of a preliminary CFD analysis performed on an innovative HAPS configuration based on the application of the hybrid concept. This configuration has a lenticular shape and it is based on a lifting body, but, unlike other configurations, its thickness is greater because a bigger volume is required to store a sufficient amount of helium to generate the required aerostatic lift and its aspect ratio is quite low.
These features make this configuration different by a standard wing or an airship which has generally an axial symmetric configuration, thus the authors have performed a preliminary CFD analysis to validate the results of the conceptual design process which is essentially based on semi-empirical formulas.
The results of the CFD have shown that the required lift can be achieved with this configuration. Future work will include the verification of static stability based on the analysis of the moment coefficients.
The analysis of the flow field will allow further improvement of the configuration in the next steps of the design process.

5. Acknowlegments

The project underlying this paper was funded by the Italian Ministry for Education, University and Research (MIUR) under the grant PON OT4CLIMA ARS01_00405.

Definitions/Abbreviations

AR = Aspect Ratio

α = angle-of-attack [degrees]

β = angle of sideslip [degrees]

C_D = drag coefficient

C_{D_0} = zero-lift drag coefficient

CFD = Computational Fluid Dynamics

CIRA = Centro Italiano Ricerche Aerospaziali/ Italian Aerospace Research Centre

C_L = lift coefficient

C_{L_α} = lift coefficient slope

C_l = rolling moment coefficient

C_M = pitching moment coefficient

C_N = yaw moment coefficient

C_Y = side force coefficient

c = chord

deg = degree

h = height

HAPS = High Altitude Pseudo-Satellite

DOI: 10.13009/EUCASS2022-4397

HTA = Highter-than-Air

l = length

LTA = Lighter-than-Air

S = in-plane wing area

SW = Software

w = width

References

[1] Baraniello V. R., Persechino G., Angelino C. V. and Tufano F. 2021 .The Application of High Altitude Pseudo-Satellites for a Rapid Disaster Response. IEEE International Geoscience and Remote Sensing Symposium IGARSS, 2021, pp. 8400-8403, doi: 10.1109/IGARSS47720.2021.9553819.

[2] Deaton J. D. 2008. High Altitude Platforms for Disaster Recovery: Capabilities, Strategies, and Techniques for Emergency Telecommunications. J Wireless Com Network. 2008:153469. https://doi.org/10.1155/2008/153469.

[3] Di Vito P., Fischer D., Rinaldo R. 2018. HAPs Operations and Service provision in Critical Scenarios. In the Proceedings of SpaceOps Conference. https://doi.org/10.2514/6.2018-2504.

[4] Alam M. S., Kurt G. K., Yanikomeroglu H., Zhu P. and Đào N. D. 2021. High Altitude Platform Station Based Super Macro Base Station Constellations. In IEEE Communications Magazine, vol. 59, no. 1, pp. 103-109. doi: 10.1109/MCOM.001.2000542

[5] J. Gonzalo, D. Lopez, D. Dominguez, A. Garcia, et alii. 2018. On the Capabilities and limitations of high altitude pseudo satellites. In the Progress in Aerospace Sciences, Volume 98, pp. 37–56.https://doi.org/10.1016/j.paerosci.2018.03.006

[6] V.R. Baraniello, G. Persechino, R. Borsa. 2020. Tools for the Conceptual Design of a Stratospheric Hybrid Platform. SAE Technical Paper 2020-01-0025, https://doi.org/10.4271/2020-01-0025

[7] L.S. Caretto, A.D. Gosman, S.V. Patankar,. D.B. Spalding. 1972. Two Calculation Procedures for Steady, Three-Dimensional Flows With Recirculation. In the proceedings of the Third International Conference on Numerical Methods in Fluid Mechanics, volume 19 of Lecture Notes in Physics, pages 60–68. Springer.

[8] OpenFOAM v6 User Guide: 5.4 Mesh generation with snappyHexMesh https://cfd.direct/openfoam/user-guide/v6-snappyhexmesh/

[9] Grant, E.C. and Leland, M.N., Fundamentals of Aircraft andAirship Design, Volume 2 - Airship Design and Case Studies, AIAA Education Series, ISBN:978-1-60086-898-6.